Journal of Engineering Science and Technology
Vol. 17, No. 1 (2022) 0404 - 0419

EXPERIMENTAL AND NUMERICAL INVESTIGATION OF LOCAL SCOUR AROUND SQUARE BRIDGE PIER

ASLI BOR*, M. ŞÜKRÜ GÜNEY

Department of Civil Engineering, Izmir University of Economics, İzmir, Turkey,
Address: Fevzi Çakmak Mahallesi, Sakarya Cd. No:156, 35330 Balçova/İzmir Turkey
*Corresponding Author: asli.turkben@ieu.edu.tr

Abstract

This study examines, local scour around square pier under unsteady flow conditions, caused by five different hydrographs. The experiments were conducted in the rectangular flume of 18.6 m length, 0.80 m width and 0.75 m depth, with uniform sediment bed material D_{50} = 1.68 mm. Five experiment series were conducted with a plexiglass square pier b = 8.5 cm. The unsteady flow was generated by means of triangular hydrographs. The temporal variations of the equilibrium scour depths in front of the pier and the scour hole dimensions were recorded by two different cameras. The equilibrium scour depths at lateral sides and downstream of the pier were also measured. The hydrograph peak flow rates were found to be much more effective compared to hydrograph durations. The numerical solution was realized by using the software ANSYS FLUENT with RNG k-ε turbulence model. The numerical and experimental values were compared and interpreted, and acceptable accordance was observed between them. The calculated lengths and widths of the scour hole were found close to the measured ones. A comparison of the final elevations (t = 15 min.) for experimental and numerical results revealed that; the values of RMSE, MAE errors, and the determination coefficient R^2 were 0.53 cm, 0.48 cm, and 0.94 respectively. The R^2 values are 0.98 and 0.95 for the measured and calculated scour hole length (L) and width (W), respectively.

Keywords: Ansys Fluent, Local scour, Pier scour, Square pier, Unsteady flows,

1. Introduction

In the literature, because of the complexity of site conditions, investigations concerning the local scour prediction are based on both dimensional analysis and laboratory experiment data [1-3]. These studies mainly focus on the maximum depth and the dimensions of the scour hole. Only limited success has been achieved by the attempts to model scour computationally. This is because studies are based mostly on equilibrium conditions under very long flow durations in clear water conditions. In fact, empirical relationships can only accurately predict the scour depths under similar conditions.

Researchers have also developed numerical methods based on computational fluid dynamics (CFD) for understanding scour mechanism [4-7]. Numerical simulations are currently complex because of the turbulence effects in practical engineering problems. Not only are three-dimensional flow and sediment transport equations nonlinear, but also unknowns outnumber the equations available, causing closure problem in turbulence modeling. Many researchers have developed two phase model techniques to investigate scouring mechanism.

Fluid - particle or particle - particle interactions can be set by Eulerian and Lagrangian frames. The set of Eulerian-Eulerian frame was introduced by Zhao and Fernando [8], and the erosion of the sedimentation was examined by Yeganeh-Bakhtiary et al. [9]. Lagrangian frame for sediment transportation was proposed by Pasiok and Stilger-Szydlo [10], and Escauriaza and Sotiropoulos [11]. Pasiok and Stilger-Szydlo developed [10] large eddy simulation (LES) model using Open FOAM CFD toolbox and FVM discretization and investigated turbulence flow around and scouring bridge piers. Escauriaza and Sotiropoulos developed DES model with Lagrangian frame and FVM discretization. Recent studies show that CFD models can be developed for sediment bed load and suspended load in unsteady and non-equilibrium conditions.

ANSYS FLUENT is a CFD modeling program for predicting three-dimensional flow field around piers which has flexible and easy deforming meshes, solving flow problems with unstructured meshes that allow generating geometries. Karim and Ali [12] developed a model using FLUENT based on conditions presented by Ali and Lim [13], and Wu and Rajaratnam [14], and compared the results with previous studies. The bottom shear stress results were adjusted using experimental data.

In 2002, Ali and Karim [15] studied the 3D flow field around a circular pier for rigid beds using FLUENT, predicted bed shear stress and performed various simulations with different time steps, comparing the results with Ettema's et al. [16] experimental data. Salaheldin et al. [17] used 3D numerical model with FLUENT to simulate the turbulent flow around vertical circular piers under clear water conditions.

Huang et al. [18] simulated a three-dimensional scour model using FLUENT and presented scale effects on turbulent flow and sediment scour. Their study was based on the Froude similarity law for the large-scale model, investigated effects of scale on turbulence flow and sediment scour by comparing results from a full-scale numerical model and from the Froude similarity method.

The main objective of this study is to analyse the scour depth and the geometry the scour hole caused by various hydrographs for a square shaped pier. The approach is based on the image processing with a video camera during unsteady

conditions. The dimensions of the scour hole were determined by using the experimental values of scour contours. In addition, numerical simulations were conducted to investigate the time dependent dimension of scour hole, the maximum scour depths, and the effect of turbulence flow in the scour hole area. The software FLUENT was used to predict the 3D flow patterns around for a square shaped pier. The experimental findings were compared with those obtained from the ANSYS FLUENT software.

2. Experimental Study

The experiments were carried out in an experimental setup located at the hydraulic laboratory of the Dokuz Eylul University in Izmir (Turkey). The system consisted of an 18.6 m long, 0.80 m wide and 0.75 m depth rectangular flume. The rectangular flume had transparent plexiglass side walls. Water was pumped from a main tank with a volume of 27 m^3. The main tank and rectangular basin were at the downstream end of the flume. The water levels can be adjusted by tail gate. To control the flow, the first part of the flume was rigid 3 meters long and 26 cm high. The test section was between 11 m and 12 m in the flume. Drive Link-C software was used to control the pump, a maximum capacity of 100 L/s and generating hydrographs by increasing and decreasing the pump speed. The uniform graded material with D_{50} = 1.68 mm was used. The geometric standard deviation was σ_g = 1.33, implying that the sediment could be assumed as being uniform, and its specific gravity was 2.65 [19].

Experiments were performed in clear water conditions. Hydrographs generated by changing the pump rotational speed are shown in Fig. 1. Discharge values were recorded during the experiments, and flow depths were measured by ULS at 7 m and 10 m of the flume. After the tests, water was gently removed from the flume without disturbing the bed topography.

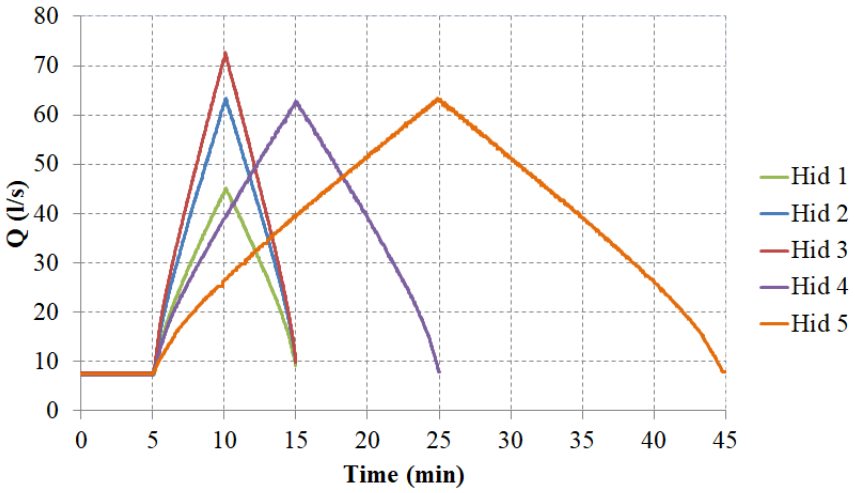

Fig. 1. Hydrographs used in the experiments.

The measurements were performed by using a laser meter and a video camera. The laser meter was used only at the end of each hydrograph when the water was

removed from the flume. The development of the scour depth was recorded by two video cameras, one located between 11 m and 12 m from the flume entrance, and the other 10th m of the flume, at an angle of 45°, in order to obtain the plan view of the pier. The first camera was mounted 41.5 cm above 80 cm × 100 cm plexiglass plate, on which 5.0 mm × 5.0 mm squares were drawn, identical to millimetric paper. This plate was 54 cm from the bed. The second camera was mounted 27 cm above 210 cm × 297 cm plexiglass plate with meshes of 5.0 mm × 5.0 mm. This plate was 120 cm from the piers. The details of this procedure are given in Fig. 2. The camera records were analysed by processing the images, and all were converted into Autocad drawings. The final state processed images were compared with Surfer topology maps. In all hydrographs, the first 5 minutes corresponds to the base flow of the hydrographs. The values of the variables characterizing the experimental conditions are summarized in Table 1.

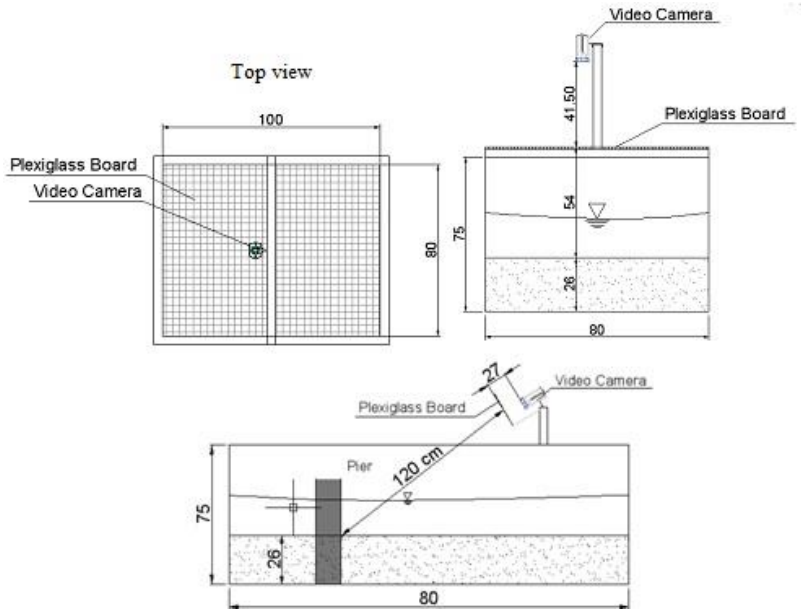

Fig. 2. Sketch to illustrate the measurement procedure by using two cameras [19].

Table 1. Experimental conditions for each experiment.

Hydrographs	Total Flow Time	Discharge Q_b - Q_p	Approach Water Depth h_b - h_p	Mean Velocity u_b -u_p	Flow Intensity Ratio I_{pb} -I_{pp}	Froude Number F_{rb} -F_{rp}
	min	**L/s**	**cm**	**m/s**		
Hid1	15	8 - 45	6 - 20.39	0.21-0.28	0.45-0.30	0.27-0.20
Hid2	15	8 - 63	6 - 22.61	0.21-0.35	0.45-0.38	0.27-0.23
Hid3	15	8 - 73	6 - 23.52	0.21-0.39	0.45-0.41	0.27-0.26
Hid4	25	8 - 63	6 - 22.61	0.21-0.35	0.45-0.38	0.27-0.23
Hid5	45	8 - 63	6 - 22.61	0.21-0.35	0.45-0.38	0.27-0.23

*The subscripts *b* and *p* denote base and peak values during hydrographs respectively.

The average flow intensity varied in the range of $0.30 < I < 0.45$, implying that the clear water scouring criterion was satisfied. The mean critical velocities u_c were calculated using the logarithmic average velocity equation (Eq. (1) [20]:

$$u_c/u_{*c} = 5.75\, log\, 5.53\, h/D_{50} \quad (1)$$

where; u_c is the mean approach critical velocity; u_{*c} is the mean approach critical shear velocity; h is the approach water depth, and D_{50} is the mean particle diameter.

Critical shear velocity u_{*c} was found by using the following equation given by Melville and Coleman [21], D_{50} being in mm. For 1 mm ≤ D_{50} ≤100 mm,

$$u_{*c} = 0.0305\sqrt{D_{50}} - 0.0065/D_{50} \quad (2)$$

The scour hole dimensions were measured at the end of each experiment. Although the scour depths were measured at different locations, the presented results are related to the midpoint of the upstream face, where the maximum scour depth was observed. A series of 5 experiments were conducted with square pier b = 8.5 cm. The time dependent scour depths for different hydrographs are given in Fig. 3. It was revealed that maximum scour depths were affected to a much greater extent by the peak flow rate values of the hydrographs than the durations of the hydrograph limbs. The final values were reached about at 60% of the hydrograph total duration. In addition, when the flow rate was increased to 63 L/s and 73 L/s, these increases caused the changes of 62% and 88% in the scour depth, respectively. When the hydrograph rising limb duration was increased to 10 min and 15 min, these increases caused changes of 0% and 15% in the scour depth, respectively [22]. The final scour hole configuration after the experiments around the pier are shown in Fig. 4, which reveals that the scours are symmetric according to the pier axis.

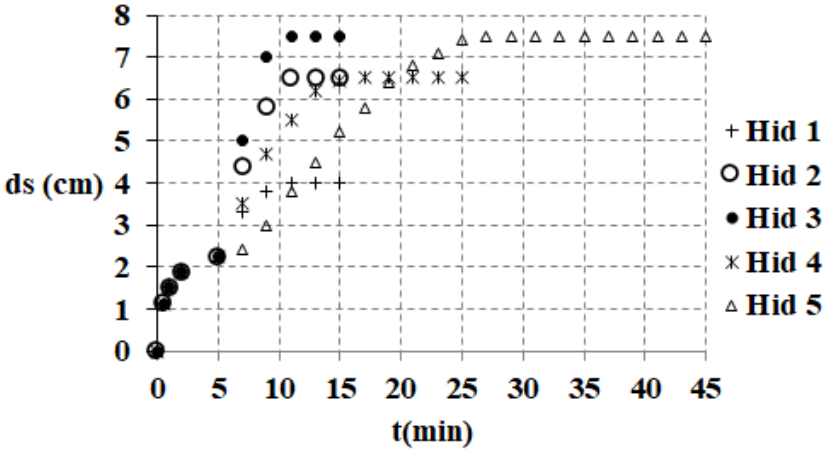

Fig. 3. Temporal variations of the scour depth [19].

The bed elevations along the centreline obtained by means of the laser meter are depicted in Fig. 5, the initial bed elevation being the datum. As shown in Fig. 5, the least deposition occurred in Hid 1, and the most, in Hid 3 and Hid 5. The observed lag results from the hydrograph duration times. Deposition occurred at downstream of the pier, the maximum being caused by Hid 5.

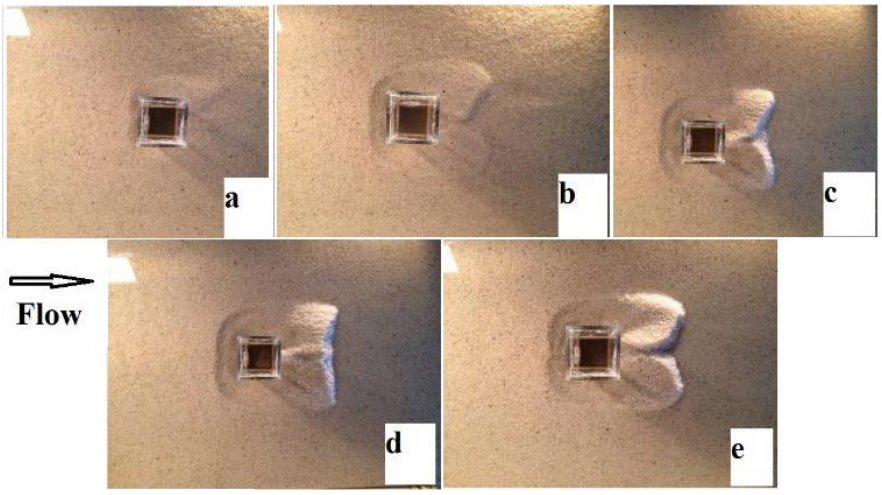

Fig. 4. Scour hole configurations at the end of each test for a) Hid 1 b) Hid 2 c) Hid 3 d) Hid 4 and e) Hid 5.

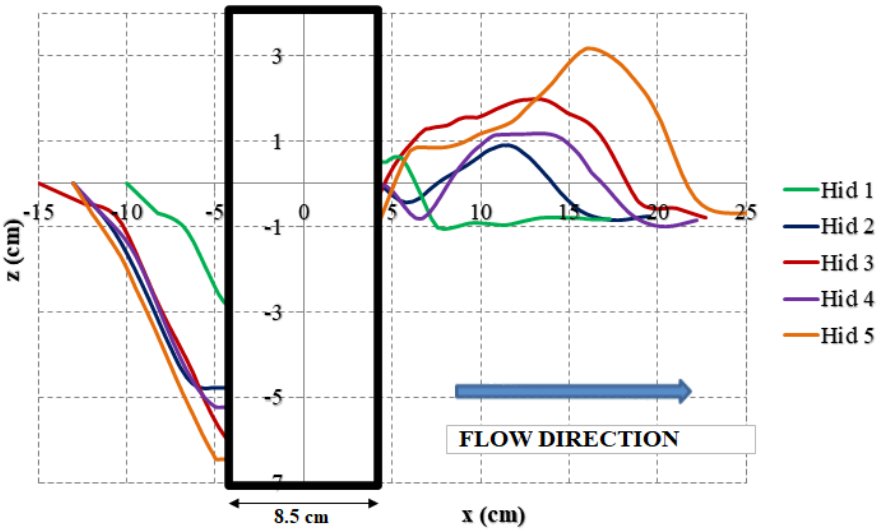

Fig. 5. Bed elevations along the centreline at the end of tests.

The final surrounding bed configurations, determined at the end of each experiment, are presented in Fig. 6. The distances are in cm. At the end of each experiment, the scour hole measurements were performed with the aid of data from the camera and laser meter, combined with Surfer software program. At upstream of the pier, it was observed that frontal scour occurred due to horseshoe vortices. At the lateral sides of the pier, the observed scouring was due to the flow separation and shear layers, and the succeeding turbulent wakes induced the deformation of the bed downstream of the pier. Also, the deposition was significant in the downstream part.

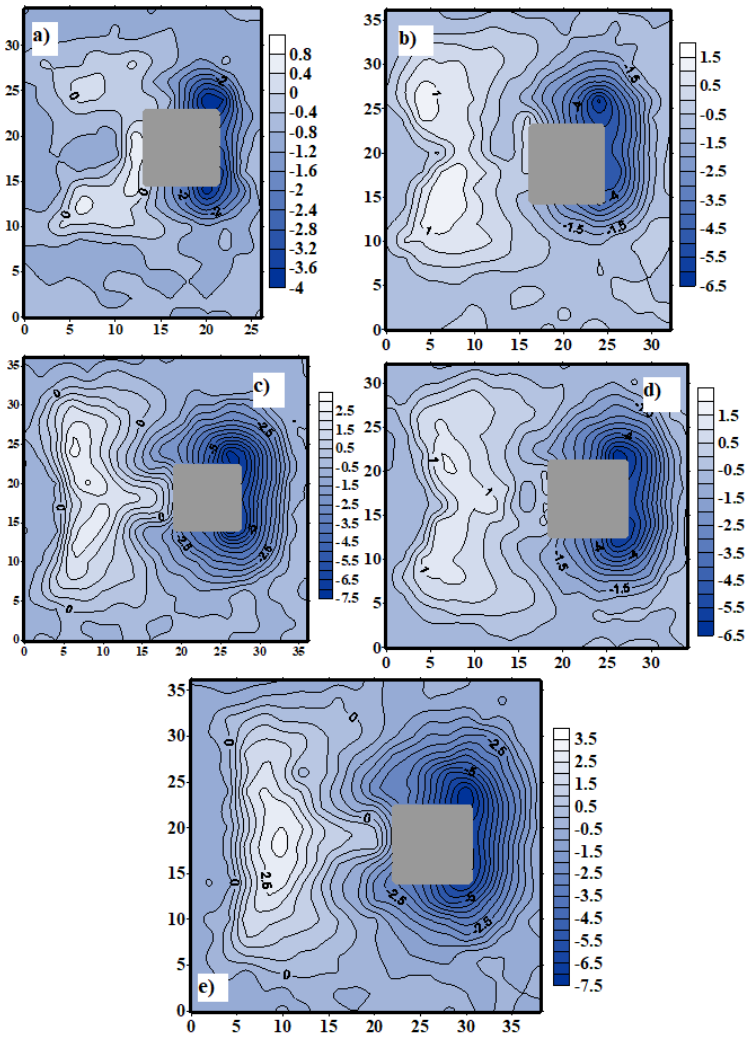

Fig. 6. Scour hole contours around the pier at the end of each test for a) Hid 1 b) Hid 2 c) Hid 3 d) Hid 4 and e) Hid 5 [19].

3. Numerical Results

Due to all limitations of traditional design methods and models, CFD is recommended because it offers a faster alternative for assessing fluid mechanics solutions. CFD has provided the basis for further insight into the dynamics of multiphase flows. There are two approaches for numerical computation of polyphase flows: Euler-Lagrange approximation and Euler-Euler approximation. The fluid phase is treated as a continuum by solving the time-averaged Navier-Stokes equations, as the dispersed phase is solved by tracking a large number of particles, bubbles, or droplets through the calculated flow field in the Euler-Lagrange approach.

The dispersed phase can exchange momentum, mass, and energy with the fluid phase, making the model unsuitable for any application where the volume fraction

of the second phase is not negligible. In the Eulerian multiphase models, fluid and sediment phases are treated mathematically as interpenetrating continua. The phases can be liquids, gases, solids or any used defined matters and their combinations. The momentum and continuity equations are solved for each phase, and a single pressure is shared by all phases. It is possible to use the parameters obtained from kinetic theory, such as shear and bulk velocities, frictional viscosity or granular temperature. In this study, the Eulerian multiphase is used to simulate scouring around piers. There are two interacting phases: water and sediment.

ANSYS FLUENT solves conservation equations for each phase. In the event of granular flows, these equations can be obtained by the application of kinetic theory. The continuity equation for phase q is:

$$\partial/\partial t\left(\alpha_q \rho_q\right) + \nabla\left(\alpha_q \rho_q \vec{V_q}\right) = 0 \tag{3}$$

where; ρ_q is the q^{th} phase density, α_q is the q^{th} phase water volume fraction, $\vec{V_q}$ is the velocity of phase q. The two-phase model includes fluid and solid (water and sediment) phases, denoted by f and s respectively in this research.

An important force is drag force, responsible for momentum exchange. In particles and particle interactions, drag coefficient gains importance when a single particle moves in a dispersed two-phase mixture. Other important forces are static pressure gradient and solid pressure gradient, viscous forces and body forces. In contrast, the component lift force can be neglected, because it relates to larger particles and virtual mass force, which is only appropriate when sediment density is much less than water density. The rate of change of momentum is equal to the resultant force acting on the control volume. The momentum balance for phase q by all assuming [23];

$$\partial/\partial t\left(\alpha_f \rho_f \vec{V_f}\right) + \nabla\left(\alpha_f \rho_f \vec{V_f}\vec{V_f}\right) = -\alpha_f \nabla P + \nabla\overline{\tau_f} + \alpha_f \rho_f g + K_{sf}\left(\vec{V_s} - \vec{V_f}\right) \tag{4}$$

$$\partial/\partial t\left(\alpha_s \rho_s \vec{V_s}\right) + \nabla\left(\alpha_s \rho_s \vec{V_s}\vec{V_s}\right) = -\alpha_s \nabla P - \nabla P_s + \nabla\overline{\tau_s} + \alpha_s \rho_s g + K_{fs}\left(\vec{V_f} - \vec{V_s}\right) \tag{5}$$

where; $\vec{V_f}$ is the velocity for fluid phase *f*, $\vec{V_s}$ is the velocity for solid phase *s*, P_s is the solid pressure for granular flows in compressible flows, P is the pressure for shared by both phases, $K_{sf}\left(\vec{V_s} - \vec{V_f}\right)$ and $K_{fs}\left(\vec{V_f} - \vec{V_s}\right)$ are the interaction forces between two phases, K_{sf} and K_{fs} are the interphase exchange coefficients, $\overline{\tau_s}$ is the stress tensor of solid phase, $\overline{\tau_f}$ is the Reynolds stress tensor for fluid phase.

3.1. Model geometry and properties

The experiments were simulated by using ANSYS FLUENT software and the relevant experimental findings were compared with those obtained from these numerical solutions. The geometry configuration of the flume is shown in Fig. 7. The grids statics were controlled by the ANSYS for good meshing. Three-dimensional grid system had 98.560 nodes and 86.073 cells with min. mesh size 5 mm, and max. mesh size 5 cm, according to ANSYS meshing generator. Then, the sediment layer of 26 cm was defined while initial and boundary conditions were given. The meshing grids for the simulation of pier are shown in Fig. 8. It can be seen that the grids near the pier are denser because this is the more complex region of the flume.

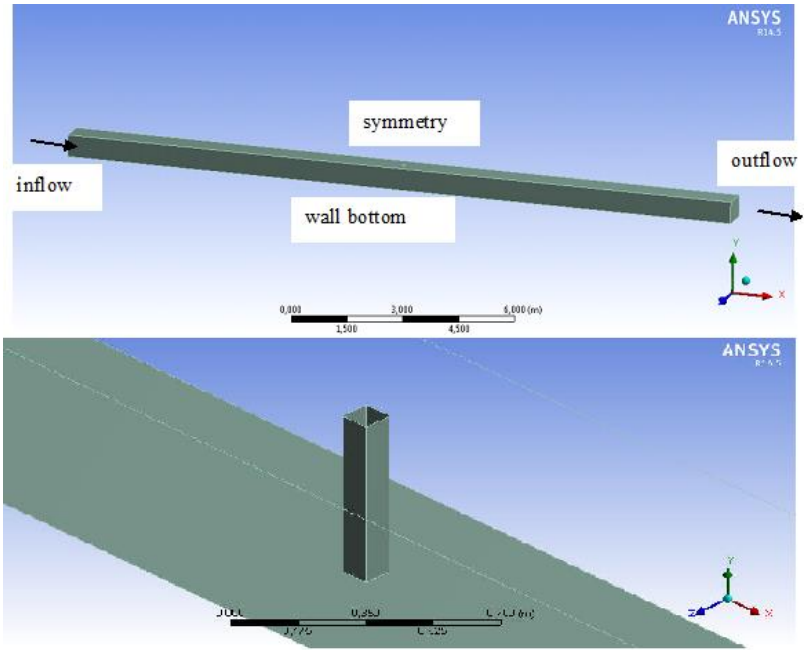

Fig. 7. Geometry configuration of flume. X is the flow direction. The gravity was set to -Y direction. The sediment layer thickness is 26 cm. The figure has no scale.

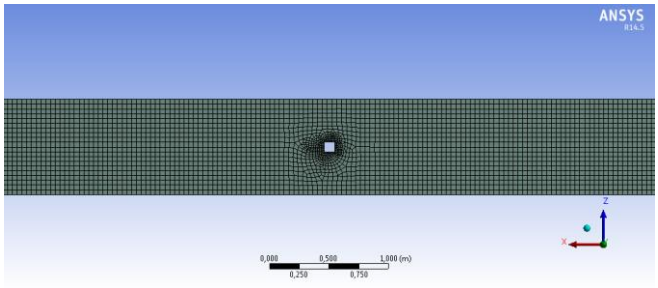

Fig. 8. Meshing grid system used in FLUENT simulations.

At the wall boundaries, no slip boundary condition was set, i.e. all velocity components were zero. The side walls and pier wall were assumed to be smooth, while the roughness height of the bottom wall was specified according to D_{50} of the sediment. In the flume domain, all velocity components were zero as initial conditions. At the inlet, the input hydrograph constitutes the upstream boundary condition. The velocity was set to *x* direction by using user defined function UDF macro. A logarithmic velocity profile was selected at the end of the inflow section while the hydrograph was passing.

At the downstream outlet, the outflow boundary condition was set, i.e. the normal gradients of all dependent variables were set zero for exit. The water surface of the flume was modelled as a symmetry plane where a zero-gradient condition was used for the velocity components parallel to the free surface, while the

gradients of k, ε and velocity components perpendicular to the free surface were set to zero. Standard wall functions were used for near wall treatment. The Gidaspow model was used to determine the water sediment exchange drag coefficient, as made by Zhao [24]. The binary turbulent diffusion coefficient was set to 0.75 as default value and particle collision coefficient was set 0.9 as recommended for sand material. The volume fraction of the sediment was patched to the adapted region before the calculation started. Density and viscosity of the water were taken as default values for 20 ºC; 998.2 kg/m^3 and 0.001003 kgm^{-1}s^{-1} respectively.

The properties of the second fluid phase sediment were defined by kinetic theory. The gravitational acceleration was taken as 9.81 m/s^2 in - y direction. The atmosphere pressure was taken as 101325 Pa for open channel flow. Defining boundary condition requires various turbulence parameters. In this study, turbulence intensity and hydraulic diameter were selected to compare the values of k and ε. Turbulence intensity, I, was defined as the ratio of the root mean square of the velocity fluctuations. An empirical formula was used to calculate the turbulence intensity [23];

$$I \equiv u'/u_{avg} = 0.16(R_e)^{-\frac{1}{8}} \quad (6)$$

where; u' is the velocity fluctuations and u_{avg} is the mean flow velocity. The solution conditions and methods are summarized in Table 2. The unsteady and implicit scheme was selected for simulations. For providing the stability conditions the Courant - Friedrichs - Lewy (CFL) condition was used. Since the water waves travel at a much higher velocity than the bed transients, this condition is given by:

$$C_n = \left(u + \sqrt{gh}\right)\Delta t/\Delta x \leq 0.25 \quad (7)$$

where; C_n is the Courant number.

Table 2. Summary of the solution conditions and methods.

Space	3D
Time	Unsteady
Turbulence model	RNG k-ε Model Standard Wall Functions Tchen Theory
Drag coefficient	Gidaspow
Viscosity model	Kinetic Theory for Sediment Phase
Pressure velocity coupling	Phase Coupled SIMPLE
Momentum	First order upwind
Volume fraction	First order upwind
Turbulence kinetic energy	First order upwind
Turbulence dissipation rate	First order upwind

4. Comparison of Experimental and Numerical Results

The interfaces between water and sediment were taken as profile, which corresponded to the sediment volume fraction α_s = 0.5. Hid 2 hydrograph was selected for simulating numerical models because it had same time lags as Hid 1 and Hid 3, and same peak discharges as Hid 4 and Hid 5. The simulated and measured scour holes configurations under Hid 2 are given in Fig. 9.

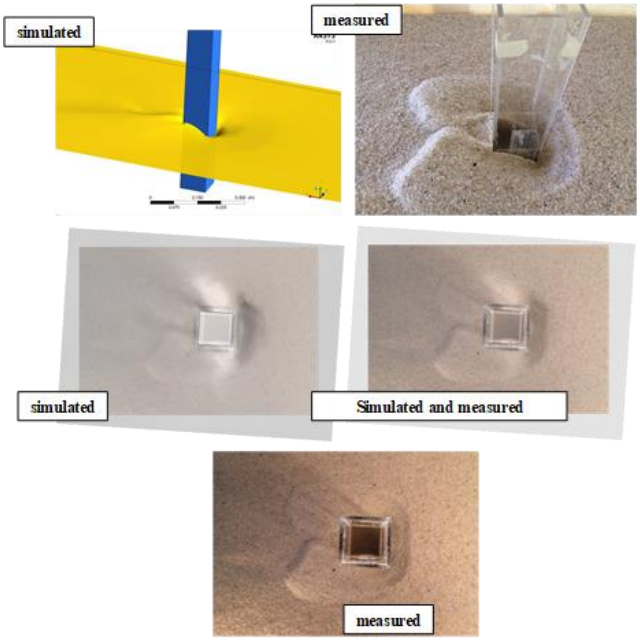

Fig. 9. Final Scour hole configurations for Hid 2.

Fig. 10 represents the model results for the variations of bed elevations of pier along the channel from the beginning of the experiment until the end of the hydrograph, involving both steady and unsteady cases. The final experimental and numerical elevations corresponding to t = 15 min are depicted in Fig. 11, which also involves the values of RMSE, MAE and the determination coefficient R^2.

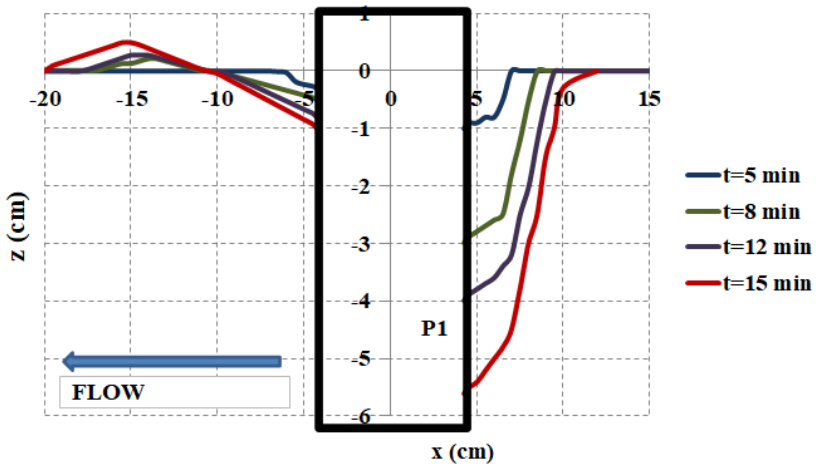

Fig. 10. Bed elevations along the channel at the region near the pier under Hid 2 conditions.

The experimental and numerical temporal variations of the maximum scour depths at the midpoint of upstream of the pier are shown in Fig. 12.

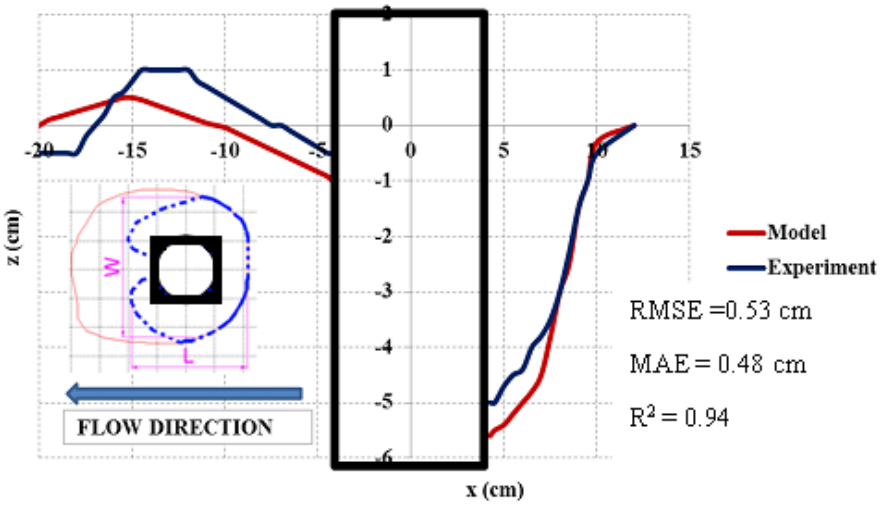

Fig. 11. Bed elevations along the channel at the region near the pier at *t* = 15 min (under Hid 2 conditions).

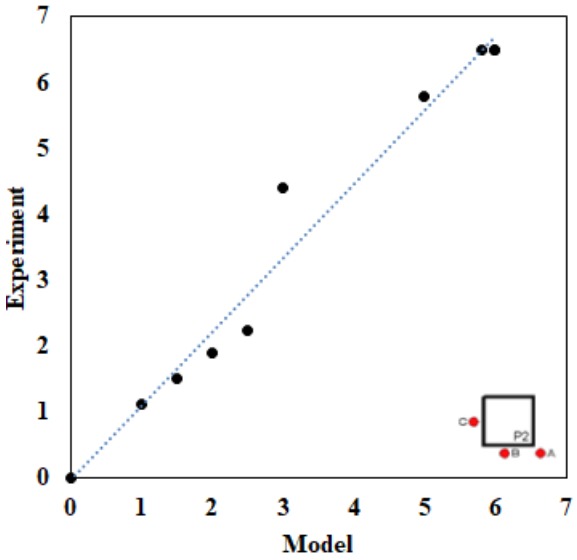

Fig. 12. Measured and simulated d_s (t) values in "cm".

The velocity vectors around square pier predicted at *t* = 5, 7, 10 and 15 min at water surface are given in Fig. 13, which also shows the simulated flow field at the water surface around the pier obtained by RNG *k*-*ε* model. Circulation and reversed flow in the immediate vicinity of the pier are clearly visible. The maximum scour depth was observed at the front corners of the pier, closely matching the experimental results. The measured and calculated values of the scour hole length (*L*) and width (*W*) are given in Table 3. The R^2 values are 0.98 and 0.95 for of the scour hole length (*L*) and width (*W*), respectively.

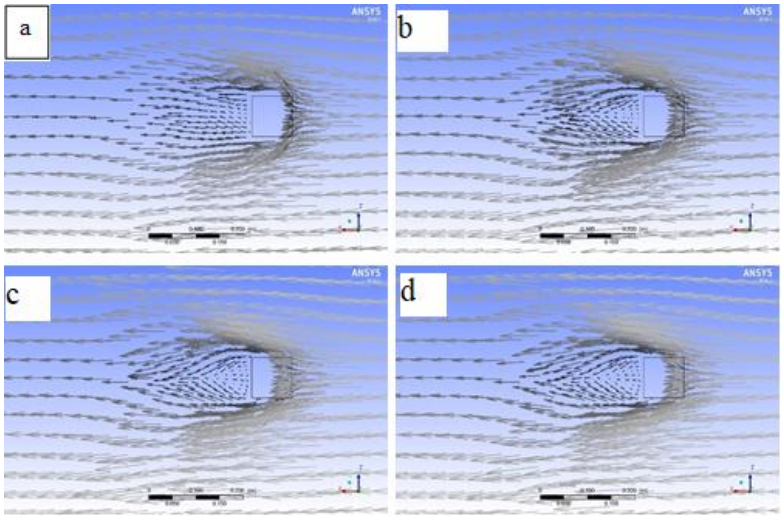

Fig. 13. Velocity vectors around the pier at a) t = 5 min, b) t = 7 min, c) t = 10 min, and d) t = 15 min.

Table 3. Measured and calculated scour length L and scour width W values.

Time (min.)	L Calculated (cm)	L Measured (cm)	W calculated (cm)	W Measured (cm)
5	9.68	10.44	15.95	16.36
10	10.9	10.66	17.05	16.36
15	15.25	13.24	20.66	21.58

The figure clearly displays circulation and reversed flow in the immediate vicinity of the pier. Figure 14 indicates velocity vectors in longitudinal section. Downward flow occurs in front of the pier, with an increase in velocity magnitude and sharper angles as the bottom was approached. Wake vortices occur in the downstream of the pier, causing deposition.

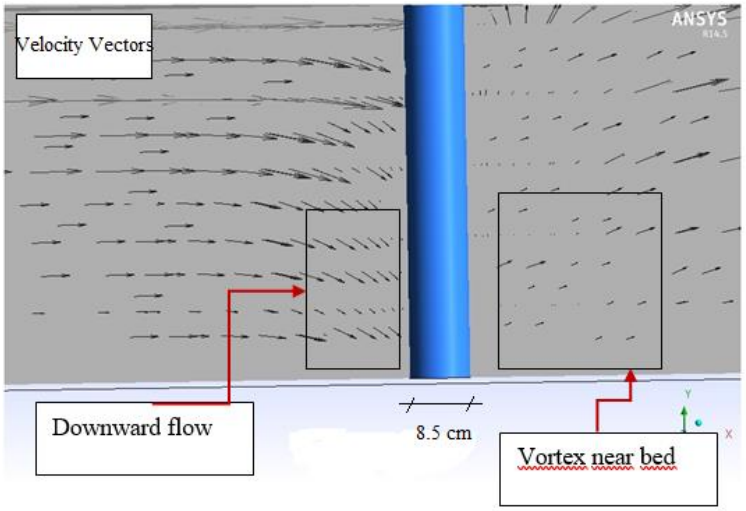

Fig. 14. Velocity vectors in longitudinal section.

5. Conclusions

The present study focuses on experimental and numerical simulation around a square pier under five different triangular shaped hydrographs. All the experiments were performed under clear water conditions, using uniform bed material. It was revealed that there were substantial differences among the scour holes, caused by hydrograph characteristics. In general, good agreement was observed between experimental findings and numerical results for scour hole geometry.

- The peak flow rates were found much more effective compared to hydrograph durations. The maximum scour depths were mainly influenced during the rising limb of the hydrographs and occurred approximately at the peak flow values. It was observed from the experiments that more than 90% of the maximum scour depth occurred just before the peak times were reached.
- An acceptable compatibility was observed between experimental findings and numerical results obtained from the software ANSYS FLUENT used with RNG k-ε turbulence model. The calculated and measured lengths and widths of the scour hole were found to be close to each other. A comparison of the final elevations (t = 15 min.) for experimental and numerical results shows that the values of RMSE, MAE, and the determination coefficient R^2 were 0.53 cm, 0.48 cm, and 0.94 respectively. The results showed that ANSYS FLUENT simulates accurately the local scouring around square pier, since R^2 values are 0.98 and 0.95 for of the scour hole length (L) and width (W), respectively.

Recommendations for future studies can be outlined as follows:

- Similar investigations can be carried out for non-uniform sediment to reveal the influence of the sediment dimension and geometric standard deviation of particle size distribution. Various shaped hydrographs may also be generated in order to study the influence of the hydrograph shapes.
- The ANSYS FLUENT software can be used with various turbulence models.

Acknowledgement

The authors would like to thank Prof. Dr. Turhan ACATAY, for his precious advice and suggestions. The authors would also like to thank Simon Edward Mumford for his help in language editing and proofreading. This study was supported by The Scientific and Technical Research Council of Turkey TUBİTAK (Project number 109M637).

Nomenclatures

b	Pier width
D_{50}	Mean particle diameter
F_r	Froude Number
h	Approach water depth
I	Intensity
K_{sf} and K_{fs}	Interphase exchange coefficients
L	Scour hole length
P	Pressure for shared by both phases
P_s	Solid pressure for granular flows in compressible flows
Q	Flow discharge
q	Phase number

R^2	Determination coefficient
t	Time
u'	Velocity fluctuations
u_{avg}	Mean flow velocity
u_c	Mean approach critical velocity
u_{*c}	Mean approach critical shear velocity
$\vec{V_f}$	Velocity for fluid phase *f*
$\vec{V_s}$	Velocity for solid phase *s*
$\vec{V_q}$	Velocity of phase *q*
W	Scour hole width

Greek Symbols

α_σ	Sediment volume fraction
α_q	q^{th} phase water volume fraction
ρ_q	q^{th} phase density
σ_g	Geometric standard deviation
$\overline{\tau_s}$	Stress tensor of solid phase
$\overline{\tau_f}$	Reynolds stress tensor for fluid phase

Subscripts

b and *p*	Base and peak values during hydrographs respectively
f and *s*	Two-phase model includes fluid and solid (water and sediment)

Abbreviations

CFL	Courant - Friedrichs - Lewy
MAE	Mean absolute error
RMSE	Root mean square error
RNG *k*-ε	RNG *k*-ε Turbulence Model

References

1. Melville, B.W.; and Chiew, Y.-M. (1999). Time scale for local scour at bridge piers. *Journal of Hydraulic Engineering*, 125(1), 59-65.
2. Chang, W.-Y.; Lai, J.-S.; and Yen, C.-L. (2004). Evolution of scour depth at circular bridge piers. *Journal of Hydraulic Engineering*, 130(9), 905-913.
3. López, G.; Teixeira, L.; Ortega-Sánchez, M.; and Simarro, G. (2014). Estimating final scour depth under clear-water flood waves. *Journal of Hydraulic Engineering*, 140(3), 328-332.
4. Olsen, N.R.B.; and Melaaen, M.C. (1993). Three-dimensional calculation of scour around cylinders. *Journal of Hydraulic Engineering*, 119(9), 1048-1054.
5. Richardson, J.E.; and Panchang, V.G. (1998). Three-dimensional simulation of scour-inducing flow at bridge piers. *Journal of Hydraulic Engineering*, 124(5), 530-540.
6. Wang, S.; and Jia, Y. (1999). Computational simulations of local scour at bridge crossings-capabilities and limitations. *Proceedings ASCE International Water Resources Engineering Conference*. Water Resources Publications, LLC, Highlands Ranch.

7. Tseng, M.-H.; Yen, C.-L.; and Song, C.C.S. (2000). Computation of three-dimensional flow around square and circular piers. *International Journal for Numerical Methods in Fluid*, 34(3), 207-227.
8. Zhao, Z.; and Fernando, H.J.S. (2008). Numerical modeling of a sagging pipeline using a Eulerian two-phase model. *Journal of Turbulence*, 9, Article N9.
9. Yeganeh-Bakhtiary, A.; Kazeminezhad, M.H.; Etemad-Shahidi, A.; Baas, L.C.; and Cheng, L. (2011). Euler-Euler two-phase flow simulation of tunnel erosion beneath marine pipelines. *Applied Ocean Research*, 33(2), 137-146. I
10. Pasiok, R.; and Stilger-Szydlo, E. (2010). Sediment particles and turbulent flow simulation around bridge piers. *Archives of Civil and Mechanical Engineering*, 10(2), 67-79.
11. Escauriaza, C.; and Sotiropoulos, F. (2011b). Initial stages of erosion and bed form development in a turbulent flow around a cylindrical pier. *Journal of Geophysical Research: Earth Surface*, 116(F3).
12. Karim, O.A.; and Ali, K.H.M. (2000). Prediction of flow patterns in local scour holes caused by turbulent water jets. *Journal of Hydraulic Research*, 38(4), 279-287.
13. Ali, K.H.M.; and Lim, S.Y. (1986). Local scour caused by submerged wall-jets. *Proceedings of the Institution of Civil Engineers*, 81(4), 607-645.
14. Wu, S.; and Rajaratnam, N. (1995). Free jumps, submerged jumps and wall jets. *Journal of Hydraulic Research*, 33(2), 197-212.
15. Ali, K.H.M.; and Karim, O.A. (2002). Simulation of flow around piers. *Journal of Hydraulic Research*, 40(2), 161-174.
16. Ettema, R.; Kirkil, G.; and Muste, M. (2006). Similitude of large-scale turbulence in experiments on local scour at cylinders. *Journal of Hydraulic Engineering* 132(1), 33-40.
17. Salaheldin, T.M.; Imran, J.; and Chaudhry, M.H. (2004). Numerical modeling of three-dimensional flow field around circular piers. *Journal of Hydraulic Engineering*, 130(2), 91-100.
18. Huang, W.; Yang, Q.; and Xiao, H. (2009). CFD modeling of scale effects on turbulence flow and scour around bridge piers. *Computers & Fluids*, 38(5), 1050-1058.
19. Bor, A.T. (2015). *Experimental and numerical study of local scour around bridge piers with different cross sections caused by flood hydrograph succeeding steady flow*. PhD Thesis, Dokuz Eylül University, İzmir.
20. Yanmaz, A.M. (2002). *Köprü hidroliği*. Ankara, Metu Press.
21. Melville, B.W.; and Coleman, S.E. (2000). *Bridge scour*. Water Resources Publications, Colorado, ABD.
22. Bor, A.; and Guney, M.Ş. (2021). Experimental investigation of scour hole characteristics for different shapes of piers caused by flood hydrograph succeeding steady flow. *Teknik Dergi*, 32(2), 10739-10766, Paper 611
23. ANSYS FLUENT 14.0 (2011). *Theory Guide*.
24. Zhao, Z. (2006). *Numerical simulation of scour around fixed and sagging pipelines using a two-phase model*. PhD Thesis, Arizona State University, Arizona.